



Modulating in-plane electron density of molybdenum diselenide via spontaneously atomic-scale palladium doping enables high performance lithium oxygen batteries



Minglu Li ^a, Chaozhu Shu ^{a,*}, Anjun Hu ^b, Jiabao Li ^a, Yu Yan ^a, Miao He ^a, Jianping Long ^{a,**}

^a College of Materials and Chemistry & Chemical Engineering, Chengdu University of Technology, 1#, Dongsanlu, Erxianqiao, Chengdu, 610059, Sichuan, PR China

^b State Key Laboratory of Electronic Thin Films and Integrated Devices, University of Electronic Science and Technology of China, Chengdu, 610054, Sichuan, PR China

ARTICLE INFO

Article history:

Received 19 August 2020

Received in revised form

4 October 2020

Accepted 6 October 2020

Available online 8 October 2020

Keywords:

Metal-air batteries
Oxygen electrodes
Catalytic activity
Palladium doping
Electronic structure

ABSTRACT

Lithium-oxygen batteries (LOBs) are considered to be one of the most competitive energy storage devices due to their high theoretical energy density. However, challenges including poor catalytic activity and durability of the oxygen electrode seriously hinder the in-depth development of LOBs. Adjusting the surface electronic structure of the oxygen electrode provides a new prospect for realizing highly efficient electrocatalysts. In this contribution, we report that atomic-scale palladium (Pd) involving in MoSe₂ (Pd–MoSe₂) is capable of adjusting the in-plane electron density of MoSe₂ via spontaneous interface chemical reactions, thereby accelerating the electron migration along the in-plane direction. The synergy between the created Se vacancies and Pd atoms can further increase the electroactive sites on the Pd–MoSe₂ surface, which is conducive to improving the catalytic activity of the electrode and thereby accelerating the kinetics of oxygen electrode reactions. The results show that Pd–MoSe₂ based LOBs exhibit excellent electrochemical performance such as high Coulombic efficiency (97.81%) as well as extended cycle life (1952 h). This work shows that the adjustment of in-plane electron density by exotic metal atom is a viable strategy to improve the catalytic activity of layered transition metal selenide, which provides the possibility of developing highly efficient electrocatalysts for LOBs.

© 2020 Elsevier B.V. All rights reserved.

1. Introduction

LOBs with ultra-high theoretical energy density (about 3505 W h kg⁻¹) are considered to be the most promising power sources for the new concept electronics and electric vehicles [1]. The reversible charge and discharge process of the batteries is based on the conversion reaction $2\text{Li} + \text{O}_2 \rightleftharpoons 2\text{Li}_2\text{O}_2$, $E^0 = 2.96 \text{ V}$ [2,3]. However, the slow kinetics of oxygen reduction reaction (ORR) and oxygen evolution reactions (OER) on oxygen electrode lead to low energy density and energy efficiency of the state-of-the-art LOBs, which seriously hinders its practical application [4,5]. Generally, the reaction kinetics of ORR and OER on the oxygen electrode can be boosted via developing highly efficient electrocatalysts, which is believed to be the most viable route to solve the

above issues [6].

Transition metal dichalcogenides (TMDs) are considered to be highly competitive electrocatalysts due to their unique layered crystal structure and adjustable surface chemistry [7–10]. In particular, MoSe₂ is considered to be one of the most promising TMDs using as catalyst [11,12], and has received extensive attention in the field of electrocatalysis [13–15]. However, it is unavoidable that the further development of MoSe₂ is limited by its limited number of intrinsic active edge sites and relatively low conductivity, which leads to sluggish kinetics of oxygen electrode reactions on MoSe₂ [16]. In recent years, researchers have adopted some innovative strategies to solve these problems, including the introduction of weak van der Waals interaction interlayers to form a single MoSe₂ layer [17]; manufacturing defects to increase reactive sites [18,19]; heterogeneous metal atom doping [20] and phase transitions engineering [21,22]. Among them, heterogeneous metal atom doping is the most effective strategy because it can adjust the electronic branch via establishing a local inherent electric field [23].

* Corresponding author.

** Corresponding author

E-mail addresses: czshu@imr.ac.cn (C. Shu), longjianping@cdu.cn (J. Long).

In general, the catalytic performance of the electrocatalyst depends mainly on the inherent activity of each electroactive site and the number of total electroactive sites [24,25]. Interestingly, the heterogeneous metal atom doping enhances the exposure of the compound's active sites and improves the intrinsic activity of each active site via adjusting the surface electron interaction [26]. Therefore, this strategy is expected to improve the catalytic activity of the MoSe₂ for oxygen electrode reactions.

In our work, palladium doping through spontaneous redox reactions is used to activate the electrocatalytic performance of MoSe₂. The atomic-scale palladium with large electronegativity can adjust the electron density near the active site on the surface of MoSe₂, creating a more favorable electron transport environment, thereby improving the catalytic activity of MoSe₂ based oxygen electrodes. In addition, since the electronegativity of Pd²⁺ is less than that of Mo⁴⁺, the binding energy of Mo⁴⁺ changes after Pd doping, which causes a negative shift of the center of the d band, thereby improving the catalytic activity. Interestingly, Pd doping occupies Mo sites and introduces Se vacancies, and the synergy of Se vacancies and Pd atoms promotes the rapid transport of electrons, thereby boosting the electrocatalytic reaction [26]. In addition, the local coulombic interaction around the atom Pd due to the introduction of uncoordinated electron spins will cause part of the surface lattice distortion, which will increase the surface unsaturation of the valence bond, promoting the effective electron transfer and increasing the number of active sites. Experimental data show that LOBs based on Pd–MoSe₂ display a large discharge capacity of 12,807 m A h g⁻¹ at a current density of 500 m A g⁻¹, a high Coulombic efficiency of 97.81% and a low overpotential of 0.47 V. More importantly, the LOBs can circulate stably for 1952 h (122 cycles) at a high cut-off capacity of 4000 m A h g⁻¹ without significant voltage attenuation. This work emphasizes the importance of adjusting the electronic structure through heterogeneous metal atom doping strategies in enhancing the electrocatalytic performance of TMD for LOBs.

2. Experimental section

2.1. Materials

The Sodium molybdate dihydrate (Na₂MoO₄·2H₂O, 99%), Selenium powder (Se, 99%), Hydrazine hydrate (N₂H₄·H₂O) and palladium acetate [Pd(OAc)₂, 99%] were purchased from Aladdin Co., Ltd. No further purification was carried out.

2.2. Synthesis of MoSe₂

0.316 g selenium powder was dissolved in 10 mL N₂H₄·H₂O, and stirred for 30 min to obtain clear solution A. Then, 0.484 g Na₂MoO₄·2H₂O was added to 50 mL deionized water and stirred to obtain transparent solution B. Under high-speed stirring conditions, solution A is slowly poured into solution B to obtain a mixed solution. The mixture was transferred to a 100 mL Teflon-lined stainless-steel autoclave and heat-treated at 200 °C for 6 h. After cooling down to room temperature, the precipitate was washed three times using deionized water and absolute ethanol, respectively, and then dried at 60 °C for 12 h. Finally, the collected powder was kept at 400 °C for 1 h under the protection of argon atmosphere to obtain MoSe₂.

2.3. Synthesis of Pd–MoSe₂

63.5 mg MoSe₂ was added to 30 mL deionized water, and a uniformly dispersed solution was obtained after sonication for 1 h. Then 30 mL 0.20 mM Pd(OAc)₂ was introduced to the obtained

homogeneous solution and stirred for 30 min to obtain Pd–MoSe₂. Finally, the prepared Pd–MoSe₂ was dried for 12 h under an environment of 60 °C.

2.4. Material characterizations

X-ray diffractometer (XRD, Bruker D8 ADVANCE) with the monochromatic Cu-K α radiation was used to obtain an X-ray diffraction spectrum. A field emission scanning electron microscope (SEM, JSM-6700F) was used to obtain the morphology of the material. Transmission electron microscope (TEM, JEOL 2100F) and atomic resolution high-angle annular dark-field scanning transmission microscope (HAADF-STEM, FEI Themis Z) were used to obtain the microstructure and lattice spacing of the material. The valence band structure of the catalyst was analyzed by UV photoelectron spectroscopy (UPS, Thermo ESCALAB 250XI). The vacancies were studied by EPR spectrometer (micro-6/1/P/L, Karlsruhe). We used nitrogen adsorption equipment (ASAP, 2010 M) to analyze the pore size distribution and specific surface area of the material. X-ray photoelectron spectroscopy (XPS, ESCALAB 250XL) was used to analyze the surface chemical environment of the material.

2.5. Electrode preparation and battery assembly

We uniformly mixed 60 wt% of the materials (Pd–MoSe₂, MoSe₂, and Super P), 10 wt% of polyvinylidene fluoride (PVDF), and 30 wt% of Super P in *N*-methyl-2-pyrrolidone (NMP) solvent to obtain an ink. After that, we evenly coated the prepared ink on the surface of the carbon cloth and dried it at high temperature under the irradiation of infrared lamps. The solvent was then removed at 60 °C for 12 h to finally obtain an electrode sheet. The as-prepared oxygen electrode, glass fiber separator, lithium anode and electrolyte (1 M LiTFSI electrolyte dissolved in ethylene glycol dimethyl ether (TEGDME)) were used to assemble LOBs in glove box filled with Ar [27–29]. Prior to testing, the assembled LOBs were placed in a closed container and purged with pure oxygen for 15 min. Constant current measurements were performed on a multi-channel battery test system (LAND CT 2001A). Cyclic voltammetry (CV) was measured using an electrochemical workstation (Metrohm Autolab, PGSTAT 302 N) with a voltage window of 2.0–4.5 V at a scan rate of 1 mV s⁻¹ [30–32]. Electrochemical impedance spectroscopy (EIS) was measured at a frequency range of 0.01–100 kHz. Among them, LAND CT 2001A battery test system was purchased from Wuhan Landian Electronics Co., Ltd., Metrohm Autolab PGSTAT 302 N electrochemical workstation was purchased from Metrohm Ltd.

3. Results and discussion

The schematic diagram of Pd–MoSe₂ synthesis strategy is shown in Fig. 1, in which three steps were included: hydrothermal method, high temperature annealing method and final impregnation process. The X-ray diffraction (XRD) pattern shows the phase composition and crystal structure of MoSe₂ and Pd–MoSe₂ nanosheets (Fig. S1). Obviously, the diffraction peaks of all synthetic samples coincide with the standard card of MoSe₂ (JCPDS 29–0914).

It is worth noting that the doping of Pd atom does not change the crystal structure of MoSe₂, which is attributed to the trace doping of Pd atom. Fig. 2a and Fig. S2 show scanning electron microscope (SEM) images of Pd–MoSe₂ and MoSe₂, it can be seen that MoSe₂ demonstrates a typical flower-like morphology. After palladium doping, Pd–MoSe₂ still maintains the flower-like morphology and no obvious agglomeration occurs, indicating that

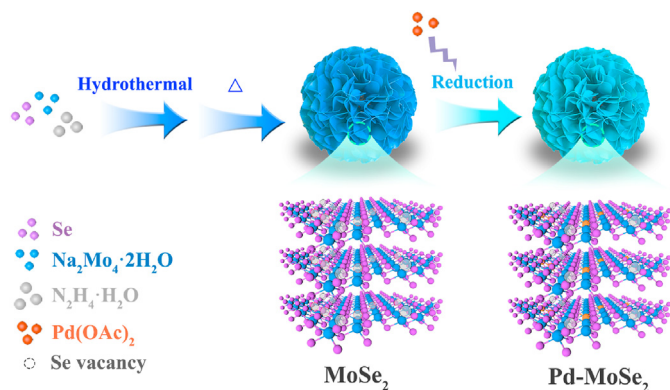


Fig. 1. Schematic of MoSe₂ and Pd–MoSe₂ synthesis strategy.

the doping of palladium does not induce observable morphological changes of MoSe₂. As shown in the transmission electron microscope (TEM) image (Fig. 2b), the flower-like porous structure of Pd–MoSe₂ composed of ultra-thin nanosheets can be more clearly observed. This unique structure is beneficial for the intimate contact between catalyst and electrolyte, thereby increasing effective reaction area. The high resolution TEM (HRTEM) image in Fig. 2c clearly shown that each of the interleaved nanosheets consists of few layers, and the layer lattice spacing is determined to be 0.64 nm, corresponding to (002) crystal plane of MoSe₂. The clear MoSe₂ lattice ensures tight interfacial contact, which provides good structural stability in repeated cycles [12]. In addition, since some molybdenum sites in Pd–MoSe₂ were replaced by palladium (Fig. S3), some selenium vacancies and defects (yellow ovals in Fig. 2c) were generated. These vacancies and defects indicate that there are many dangling bond unsaturated sites, which may accelerate the transport rate of electrons and reduce their surface energy, thereby promoting the electrocatalytic process [33,34]. The selected area electron diffraction (SAED) pattern of Pd–MoSe₂ is shown on the inset of Fig. 2c. The existence of distinct diffraction rings corroborates the good crystallinity of Pd–MoSe₂. And the

diffraction spots marked from the inside out correspond to (002), (100), (103) and (110) planes of MoSe₂, respectively. Fig. 2d reveals the honeycomb lattice structure of Pd–MoSe₂ with triangular prism coordination, which is a typical 2H phase structure. From Fig. 2e, we can see that after Pd fixture in the MoSe₂, MoSe₂ still maintains an ordered crystal structure, proving that Pd is doped in atomic form [20]. In addition, it is also proved in Figs. S4a and b that there are some defects (yellow ellipse) in Pd–MoSe₂, which is consistent with the HRTEM results. As analyzed above, the presence of defects can boost both the electron transport rate and the reaction kinetics. The energy dispersive spectroscopy (EDS) element mapping of Pd–MoSe₂ (Figs. 2f and S5) indicates that Pd is uniformly doped in MoSe₂. Proportion of element of Pd–MoSe₂ determined by EDS is listed in Table S1. The content of palladium atom in Pd–MoSe₂ is 6.86% (Table S2), which is quantified by using ICP-AES.

In general, MoSe₂ prepared by chemical methods has a certain amount of defects, causing the deviation of actual stoichiometric ratio of Mo and Se from the theoretical stoichiometric ratio of 1: 2. ICP-AES was further used to determine the ratio of Mo and Se in MoSe₂ and the result shows that the molar ratio of Mo to Se synthesized in our work is about 1: 1.99 (Table S3), therefore the average valence of Mo is about 3.98. Moreover, the valence state of Mo ion in MoSe₂ was analyzed through the high-resolution Mo 3d X-ray photoelectron spectroscopy (XPS) to corroborate the favorable formation of vacancies during Pd doping. The Mo 3d XPS results in Fig. S6 visually demonstrate the presence of two valence states (Mo³⁺ and Mo⁴⁺). The deconvoluted doublet is clearly assigned to Mo³⁺ (3d_{3/2} at 232.3 eV and 3d_{5/2} at 229.1 eV) and Mo⁴⁺ (3d_{3/2} at 233.3 eV and 3d_{5/2} at 229.3 eV), respectively. According to the principle of charge conservation, the mixed valence of Mo ions can enhance the redox ability of MoSe₂ [35]. Thus, when Pd²⁺ is introduced, Pd²⁺ and Mo³⁺ undergo a redox reaction to generate Pd atoms and Mo⁴⁺, leading to the formation of Mo vacancies due to the oxidation of Mo³⁺. In addition, palladium in metallic state is thermodynamically favored to anchor to high energy Mo vacancies and is thus doped into MoSe₂ by spontaneously forming a more stable Pd–Se bond. Furthermore, by increasing the number of

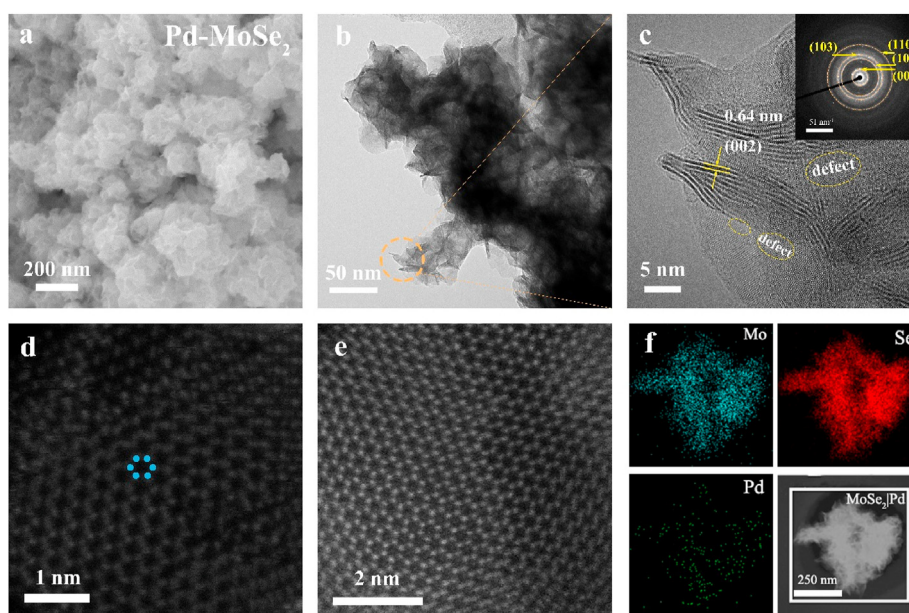


Fig. 2. Surface Morphology of Pd–MoSe₂. a) SEM, b) TEM and c) HRTEM images of Pd–MoSe₂. Inset in c) shows the SAED pattern of Pd–MoSe₂. d) and e) STEM-HAADF of Pd–MoSe₂. f) EDS element mapping of Pd–MoSe₂.

electrons during the Mo vacancy formation, Pd–Se bonds can be easily formed, which will lead to the leaching of some Se and the formation of Se vacancies in the solution according to the principle of charge conservation [20]. Moreover, The XPS spectra of Pd–MoSe₂, Pd(OAc) and PdO are shown in Fig. S7. Proportion of each element of Pd–MoSe₂ determined by XPS is listed in Table S4. Based on the analysis of Fig. S8, it can be seen that Pd–MoSe₂ ($\phi_1 = 1.9$ eV) has a lower work function than MoSe₂ ($\phi_2 = 4.1$ eV), implying that the electronic structure of MoSe₂ after Pd doping has been optimized and the electron transport efficiency has been improved [36]. The effect of palladium doping on Se vacancies was studied by electron paramagnetic resonance (EPR) spectroscopy, and the signal intensity ($g = 2.0039$) reflected the concentration of unpaired electron. It can be found that the concentration of Se vacancies increase significantly after Pd atom doping. Se vacancies will increase unsaturated bonds and improve the electrical activation of MoSe₂, thereby accelerating the migration of electrons in favor of the reversible decomposition of Li₂O₂ [37]. The N₂

adsorption-desorption isotherm was shown in Fig. 3b and Fig. S9. It can be clearly seen that the adsorption and desorption curves of Pd–MoSe₂ and MoSe₂ are typical type IV curves and H3 type hysteresis loops. The Specific surface areas of Pd–MoSe₂ and MoSe₂ are 60.84 m² g⁻¹ and 30.76 m² g⁻¹, respectively. As shown in the insets in Fig. 3b and Fig. S9, the average pore sizes of Pd–MoSe₂ and MoSe₂ are 6.53 nm and 6.66 nm, respectively, indicating the mesoporous characteristics. This type of porous structure can provide abundant active centers for the oxygen redox reactions [38]. The surface chemistry of Pd–MoSe₂ and MoSe₂ was compared, as shown in Fig. 3c. The 3d_{5/2} peak of Mo³⁺ in Pd–MoSe₂ is negatively shifted by 0.15 eV compared with that in MoSe₂. Moreover, the 3d_{3/2} peak of Mo³⁺, the 3d_{5/2} peak and the 3d_{3/2} peak of Mo⁴⁺ in Pd–MoSe₂ are negatively shifted by 0.33eV, 0.08eV and 0.39eV, respectively due to the fact that the electronegativity of Pd²⁺ is less than that of Mo⁴⁺, which leads to a negative shift of the binding energy [39]. In addition, two peaks at 54.81 eV and 55.66 eV can be assigned to Se 3d_{5/2} and 3d_{3/2} of MoSe₂, respectively, in Se 3d XPS

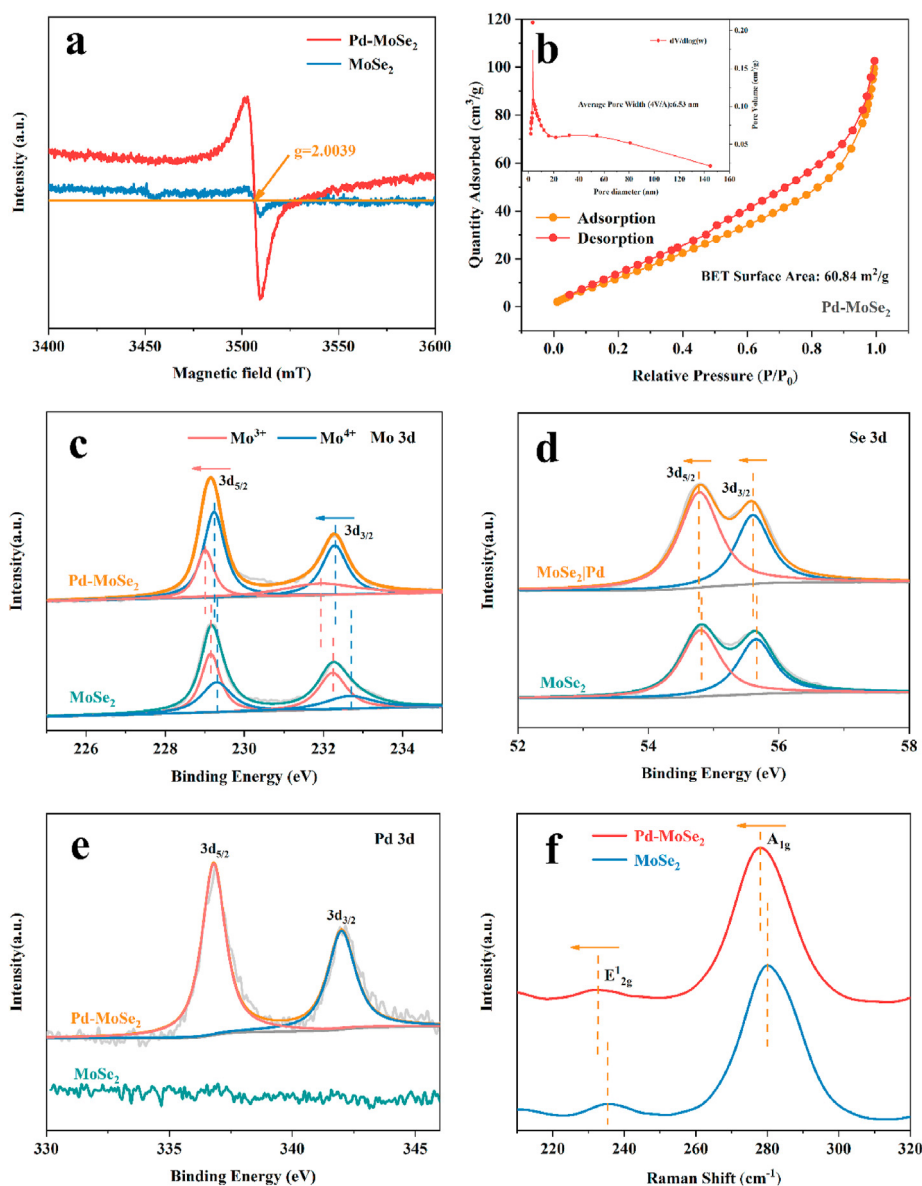


Fig. 3. Characterization of Pd–MoSe₂ and MoSe₂. **a)** EPR spectra of the Pd–MoSe₂ and MoSe₂. **b)** N₂ adsorption-desorption isotherms of Pd–MoSe₂. Inset in **b)** shows the pore size distribution of Pd–MoSe₂. **c)** Mo 3d, **d)** Se 3d and **e)** Pd 3d XPS of Pd–MoSe₂ and MoSe₂. **f)** Raman spectra of Pd–MoSe₂ and MoSe₂.

(Fig. 3d). Compared with MoSe₂, the Se 3d_{5/2} peak of Pd–MoSe₂ is negatively shifted by 0.03 eV and the Se 3d_{3/2} peak is shifted by 0.06 eV. It is possible to attribute the negative shift of Mo³⁺/Mo⁴⁺ and Se 3d to the electronegativity of Pd²⁺ being less than Mo³⁺. After Pd doping, the d-band electron configuration of the metal center in MoSe₂ can be further redistributed to form a new spin-polarized band, thereby enhancing the co-electron capability of adjacent metal centers and increasing the electron transfer rate [39]. In the Pd 3d fine spectra, two distinct peaks at 336.82 eV and 342.02 eV can be found for Pd–MoSe₂, which correspond to Pd 3d_{5/2} and 3d_{3/2}, further indicating the successful doping of Pd in MoSe₂. By analyzing Fig. 3f, the vibrational peak at 280.19 cm⁻¹ in the Raman spectra can be assigned to the in-plane vibration (E_{12g}) of the Mo and Se atoms in MoSe₂, and the vibrational peak at 235.38 cm⁻¹ corresponds to the out-of-plane vibration (A_{1g}) of the Se atom in MoSe₂ [40]. Compared with MoSe₂, the E_{12g} peak and A_{1g} peak of Pd–MoSe₂ were negatively shifted by 2.11 cm⁻¹ and 2.79 cm⁻¹, respectively. This may be due to the local Coulombic interaction around the Pd atom caused by the introduction of non-coordinating electron spins. The local Coulombic interaction implies the presence of abundant dangling bonds, promising to reduce the surface energy of the catalyst and increase the number of active sites [34].

In order to study the effect of metal element doping on the catalytic performance of MoSe₂, Pd–MoSe₂ and MoSe₂ were used as oxygen electrodes for LOBs. For comparison, Super P based oxygen electrode was prepared and tested under the same conditions to exclude the effects of Super P presented in the Pd–MoSe₂ and MoSe₂ oxygen electrodes. As shown in Fig. 4a, LOBs were subjected to the first discharge-charge test at the voltage range of 2–4 V with a current density of 500 mA g⁻¹. The discharge platform of Pd–MoSe₂ oxygen electrode is about 2.71 V and the charging platform is about 3.49 V. Compared with MoSe₂ and Super P based LOBs, Pd–MoSe₂ based LOB has a higher discharging platform and a lower charging platform. Moreover, the Pd–MoSe₂ based LOB shows large discharge capacity (about 12,807 mA h g⁻¹) and high Coulombic efficiency (about 97.81%). By contrast, the specific capacity and Coulombic efficiency of MoSe₂ and Super P based LOBs are 7340 mA h g⁻¹ and 68.05%, 4129 mA h g⁻¹ and 31.33%, respectively. The rate performance of the LOBs based on Pd–MoSe₂, MoSe₂ and Super P at the same limit capacity (1000 mA h g⁻¹) and different current densities (100, 200, 300, 400 and 800 mA g⁻¹) are shown in Fig. 4b–d. At a high current density of 800 mA g⁻¹, the overpotential of the LOB with Pd–MoSe₂ electrode is only 0.37 V, which is significantly lower than that of MoSe₂ and Super P based LOBs (0.65 V and 0.72 V, respectively). Moreover, when the current density increases, the discharge platform and charge platform of Pd–MoSe₂ are almost stable, showing outstanding rate capability of Pd–MoSe₂ based LOB. After discharge and charge at 800 mA g⁻¹, the current density was restored to 100 mA g⁻¹ to study the restorability of different electrodes. Obviously, compared with MoSe₂ and Super P oxygen electrodes, the Pd–MoSe₂ oxygen electrode has smaller overpotential and better restorability. Cyclic voltammetry (CV) curves of the LOBs (Fig. S10) were measured at a scan rate of 1 mV s⁻¹ with a voltage windows of 2–4.5 V. A reduction peak appears at 2.34 V in the negative sweep region, which can be interpreted as the generation of Li₂O₂ during the discharge of LOB with Pd–MoSe₂ oxygen electrode. An oxidation peak appears at 4.13 V in the positive scan region, which is caused by the decomposition of the Li₂O₂ [41]. In contrast, no oxidation peak and reduction peak can be found for the LOB with MoSe₂ electrode, indicating the improved reaction kinetics of MoSe₂ after Pd doping. In addition, electrochemical impedance spectroscopy (EIS) tests were conducted on the LOBs with Pd–MoSe₂, MoSe₂ and Super P electrodes (Fig. S11), and the results were fitted according

to the equivalent circuit diagram (inset in Fig. S11). The diameter of the semicircle in the intermediate frequency region of Pd–MoSe₂ oxygen electrode is obviously smaller than that of MoSe₂ and Super P oxygen electrodes, indicating that palladium doping enhances the exposure of active sites and regulates the electronic interaction, thereby improving its catalytic activity and the reaction kinetics of oxygen redox reactions. The fitted results (Table S5) show that the charge transfer resistance (R₂) of Pd–MoSe₂ electrode is 80.28 Ω, and that of MoSe₂ and Super P electrodes are 110.80 Ω and 136.40 Ω, respectively. Electronic conductivities of prepared samples of three oxygen electrodes are listed in Table S6. In order to further research the effect of the introduction of Pd on the electrochemical performance of MoSe₂, the cycle performance of LOBs based on Pd–MoSe₂, MoSe₂ and Super P oxygen electrodes were compared at a current density of 500 mA g⁻¹ with a limited specific capacity of 4000 mA h g⁻¹ (four times the conventionally limited specific capacity). As shown in Fig. 4e, the discharge voltage of the LOB with Pd–MoSe₂ oxygen electrode remains stable for 1952 h (122 cycles). In contrast, LOBs with MoSe₂ and Super P oxygen electrodes have obvious voltage attenuation during cycling and the terminal voltages suddenly drop below 2.0 V after 86 and 62 cycles for MoSe₂ and Super P oxygen electrodes, respectively. In addition, we drew a Ragone plot (Fig. S12) of LOBs based on Pd–MoSe₂, MoSe₂ and Super S oxygen electrodes. The results show that Pd–MoSe₂ demonstrates excellent energy density and power density. In order to more objectively evaluate the catalytic performance of the Pd–MoSe₂ oxygen electrode, we compare the cycle performance of LOBs studied in this work with previous results (Fig. S13). The results show that the LOB based on Pd–MoSe₂ oxygen electrode demonstrates improved cycle performance.

So as to study the origin of the performance improvement of the LOB with Pd–MoSe₂, the surface composition of the oxygen electrode under different states were analyzed. As shown in Fig. S14a, the Li₂O₂ characteristic peaks at 32.78°, 34.83°, and 58.51° of the discharged Pd–MoSe₂ oxygen electrode are not obvious and cannot be distinguished from the noise ratio. Therefore, the discharge product on the Pd–MoSe₂ oxygen electrode may be amorphous Li₂O₂. In contrast, the new peaks of discharged MoSe₂ electrode can be observed (Fig. S14b), which is highly consistent with the standard XRD card of Li₂CO₃ (PDF#22–1141). As shown in Fig. S14c, the XRD peak of the product cannot be clearly discerned for the discharged Super P electrode due to the strong C peak. Raman and XPS analysis were performed on the three oxygen electrodes after discharge and charge to further study the surface states of the electrodes at different stages. The Raman peak of the discharged Pd–MoSe₂ electrode (Fig. 5a) at about 800 cm⁻¹ could be attributed to the formation of Li₂O₂ [42]. The peak disappeared after charging, indicating that Li₂O₂ was completely decomposed on Pd–MoSe₂ electrode. The peaks at about 1352 cm⁻¹ and 1580 cm⁻¹ correspond to peaks of C due to the conductive agent in the Pd–MoSe₂ electrode [43]. For the MoSe₂ electrode (Fig. 5b), the Raman peak measured at about 1088 cm⁻¹ after discharge corresponds to the formation of Li₂CO₃ [44]. The peak disappeared after charging, which may be due to the decomposition of crystalline Li₂CO₃ under high charge voltage. Because the intensity of the C peak is too high in the Raman spectrum of the discharged and charged Super P oxygen electrode (Fig. S15), the peak of the surface species cannot be observed. Fig. 5c shows the XPS spectrum of the Pd–MoSe₂ oxygen electrode after discharge and charging. The peak appearing at 54.7 eV after discharge corresponds to Li 1s, suggesting the formation of Li₂O₂ [45]. According to the analysis of the discharged Pd–MoSe₂ in Fig. 5a, it can be seen that the discharge product is Li₂O₂ and there is no Li₂CO₃. Therefore, the peak that appears at 55.86 eV after charging (Fig. 5c) corresponds to Se 3d instead of Li₂CO₃. The peak of Li₂O₂ disappears after charging, which indicates

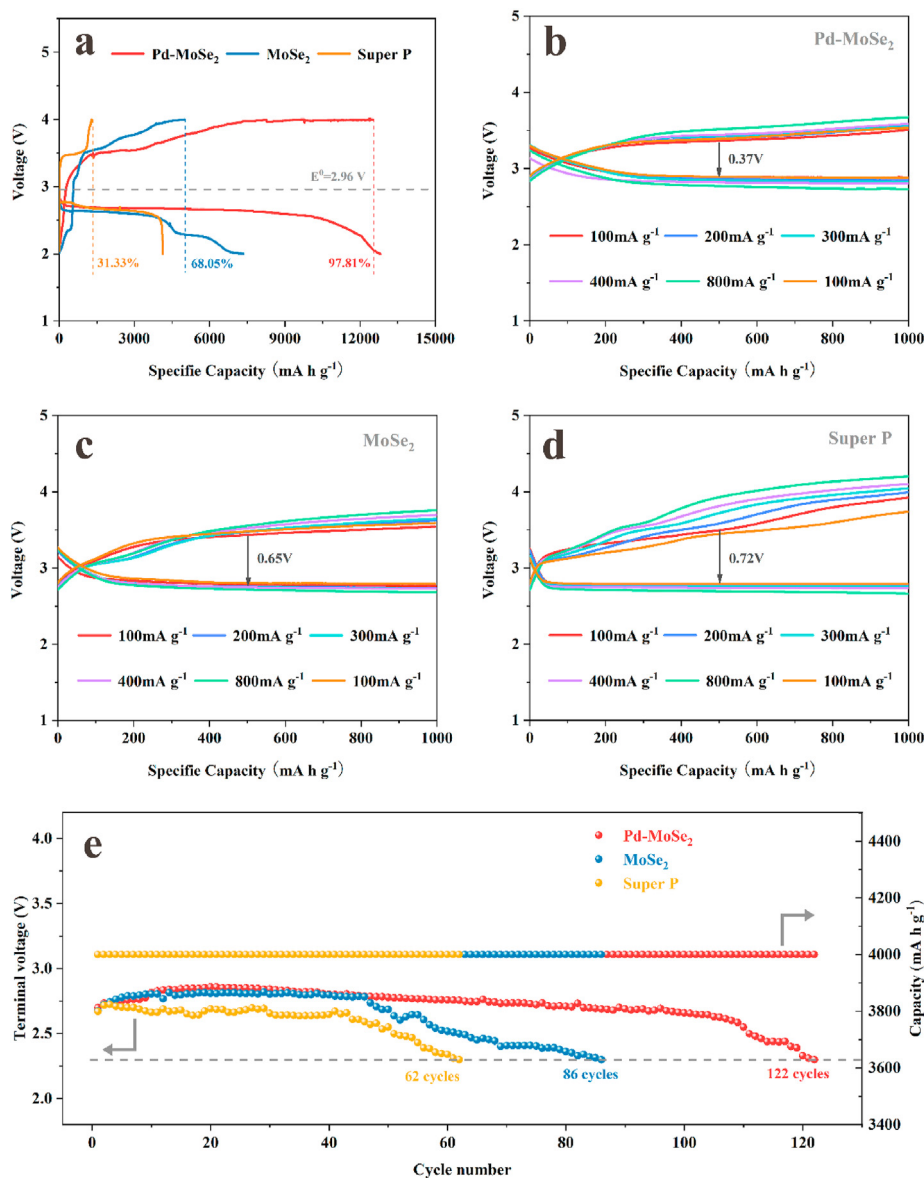


Fig. 4. Electrochemical performance of LOBs with Pd–MoSe₂, MoSe₂ and Super P oxygen electrodes. **a)** First discharge and charge curves at a current density of 500 mA g⁻¹. Rate capability of **b)** Pd–MoSe₂, **c)** MoSe₂ and **d)** Super P oxygen electrodes. **e)** Cyclic performance of LOBs measured at a current density of 500 mA g⁻¹ and an ultimate capacity of 4000 mA h g⁻¹.

that Li₂O₂ is completely decomposed. Raman and XPS results prove that Li₂O₂ is the discharge product and can be formed and decomposed reversibly during the discharge–charging process for LOBs based on Pd–MoSe₂. Raman and XPS results prove that Li₂O₂ is the discharge product on the Pd–MoSe₂ oxygen electrode, and is formed and decomposed reversibly during discharge and charging. This result also confirms the above speculation that the discharge product on the Pd–MoSe₂ oxygen electrode is amorphous Li₂O₂. Amorphous products are more conducive to decomposition and thus demonstrate high reversibility.

In contrast, as shown in Fig. 5d, the MoSe₂ oxygen electrode shows a peak at 55.9 eV after discharge and at 55.4 eV after charging, which can be assigned to Li₂CO₃ [45,46]. Similarly, as shown in Fig. S16, peaks belonging to Li₂CO₃ appear at 55.5 eV and 56.2 eV, respectively, after discharging and charging on the Super P oxygen electrode. The results of XPS indicate that the main discharge products on the surface of MoSe₂ and Super P electrodes

are Li₂CO₃. After charging, this by-product cannot be completely decomposed, which exacerbates the premature aging of LOBs.

In order to more intuitively observe the formation and decomposition of the products, morphology characterization on the three electrodes at different stages was carried out, as shown in Fig. 6. Because both the binder and conductive agent are present in the electrodes, the initial morphology of the electrodes are similar and they are small particles bonded together (Fig. 6a, d and g). After discharging, the flaky product appeared on the Pd–MoSe₂ electrode (Fig. 6b). According to the Raman and XPS analysis above, we can assign this product to Li₂O₂. After charging, all the flaky products disappeared, and the electrode recovered its original morphology (Fig. 6c), which illustrates the reversible formation and decomposition of the discharge products on the electrode surface during the discharge and charging process of LOBs with Pd–MoSe₂. In Fig. 6e, it can be seen that spherical particles appear on the MoSe₂ electrode after discharging, but some spherical particles

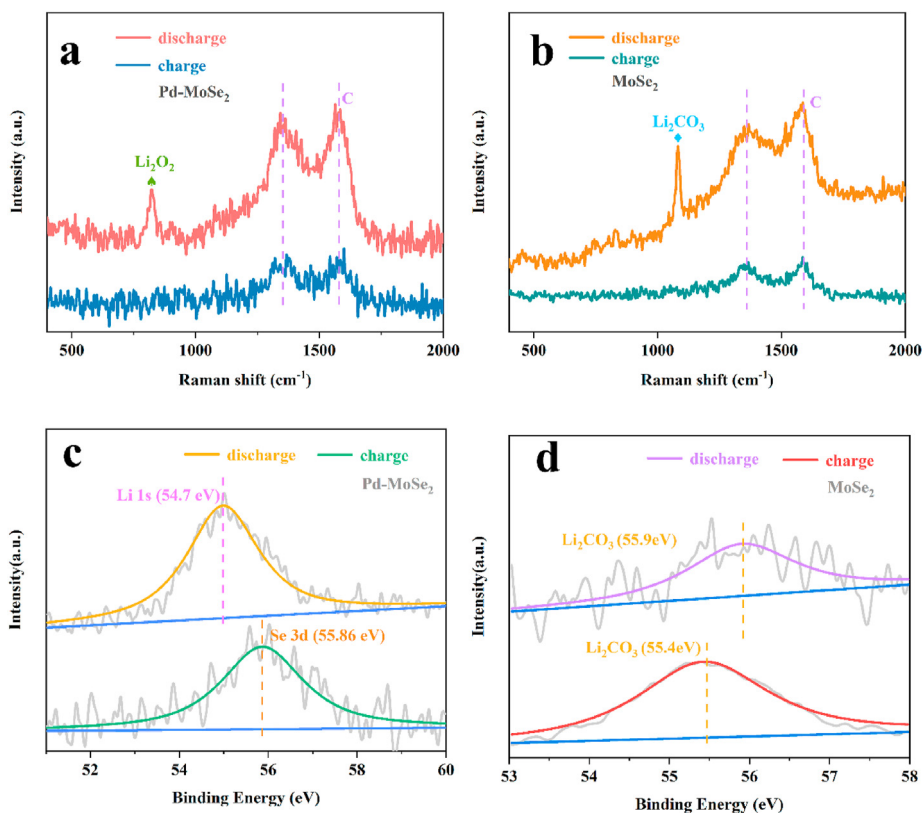


Fig. 5. Raman spectra of **a)** the Pd–MoSe₂ electrode and **b)** MoSe₂ electrode after discharging and charging. XPS spectra of **c)** the Pd–MoSe₂ electrode and **d)** MoSe₂ electrode after discharging and charging.

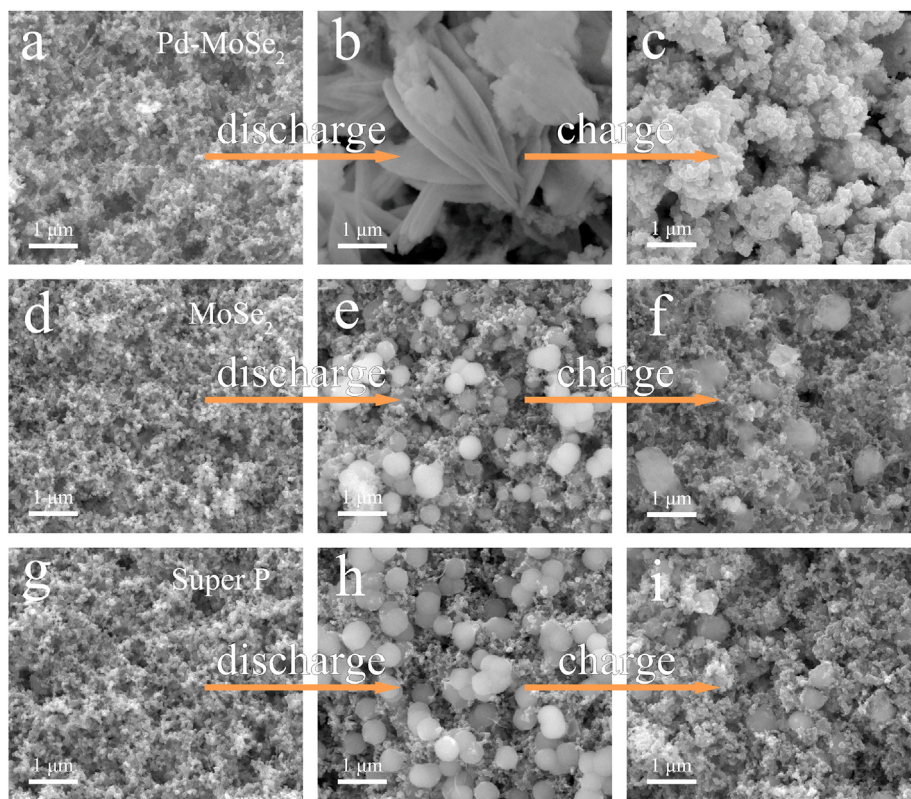


Fig. 6. SEM images of (a–c) Pd–MoSe₂ electrode, (d–f) MoSe₂ electrode and (g–i) Super P electrode at (a, d, g) the initial state, (b, e, h) discharged state and (c, f, i) recharged state.

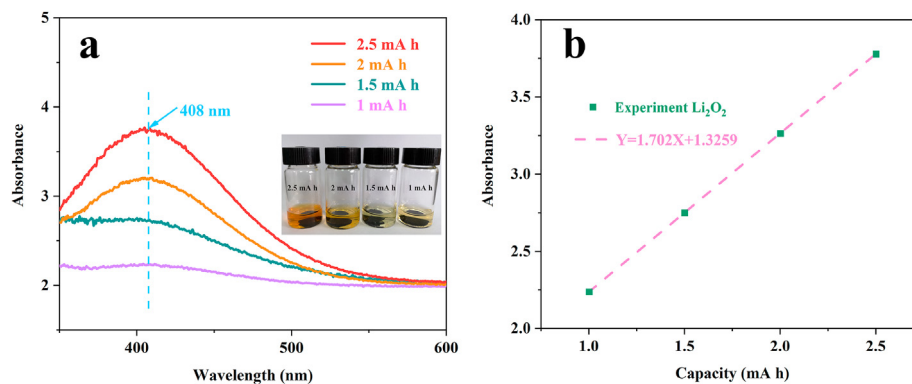


Fig. 7. a) The UV–Vis spectra of titration solution with Pd–MoSe₂ electrodes at different discharge capacity. The inset is the optical image of TiOSO₄ solutions with the discharged Pd–MoSe₂ electrodes. b) The corresponding Lambert-Beer plot.

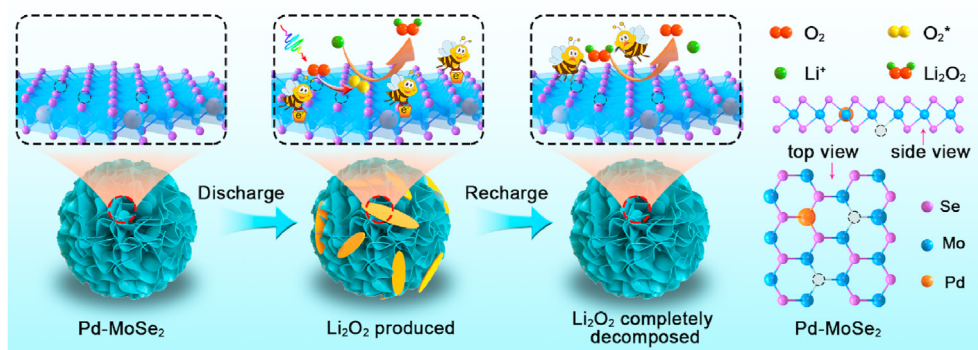


Fig. 8. A conceptual illustration of the formation and decomposition of Li₂O₂ on Pd–MoSe₂ electrode.

remained after charging (Fig. 6f). It can be understood that the product formed on the surface of the MoSe₂ electrode after discharging will not be completely decomposed after charging. In addition, according to the Raman and XPS analysis (vide supra), Li₂CO₃ by-products can be produced on the MoSe₂ electrode after charging, which will hinder the reversible discharge-charge process of LOBs and reduce the cycle life of MoSe₂ based LOBs. As shown in Fig. 6h, dense spherical particles appear on the Super P electrode surface after discharging, and there are still many undecomposed spherical particles after charging, indicating that the discharged product is irreversibly formed and decomposed on the Super P electrode. Compared with MoSe₂ and Super P oxygen electrodes, Pd–MoSe₂ oxygen electrode demonstrates much better capacity for reversible formation and decomposition of discharge products, which can be attributed to the modulated electronic structure on the material surface after palladium atom doping due to the large electronegativity of palladium atom as compared to that of molybdenum atom. Through using palladium as a regulator, the electron density of the catalytic sites of the MoSe₂ nanoarray is adjusted, thereby improving the electrocatalytic performance of the oxygen electrode and accelerating the redox reaction process on the electrode surface.

The electrochemical impedance spectroscopy (EIS) in Fig. S17 a–c were used to further analyze the discharge and charge states of the three electrodes. After the first discharge, the diameter of the semicircle of the three electrodes in the intermediate frequency region increased significantly, indicating the increase of the charge transfer resistance. We attribute this to the generation of insulated Li₂O₂ covering on the electrode surface during the discharge. Interestingly, the charge transfer resistance of the Pd–MoSe₂

electrode can be restored to almost the initial state after charging, because of the complete decomposition of Li₂O₂. In contrast, after charging MoSe₂ and Super P electrodes, charge transfer resistance is significantly larger than the initial state, indicating that the discharge products cannot be completely decomposed, and there are still remnants with poor conductivity on the electrode surface, which reduces the electron transport.

The amount of Li₂O₂ produced on discharged Pd–MoSe₂ electrode can be accurately quantified by analyzing the TiOSO₄ titration solution with the discharged electrode sheet using ultraviolet–visible (UV–Vis) spectra. Under Ar atmosphere, the oxygen electrodes with different discharge capacities are quickly placed into the TiOSO₄ solution. H₂O in the solution will react spontaneously with the discharged product Li₂O₂ on the electrode to generate H₂O₂. Subsequently, TiOSO₄ reacts with H₂O₂ to form H₂ [Ti(O₂) (SO₄)₂]. The chemical equation is as follows: H₂SO₄ + H₂O₂ + TiOSO₄ → H₂O + H₂ [Ti(O₂) (SO₄)₂]. When the oxygen electrode was placed in the TiOSO₄ solution, the color of the titration solution instantaneously changed from transparent to orange–yellow, which was due to the formation of H₂ [Ti(O₂) (SO₄)₂] [18,36]. Li₂O₂ generated on the oxygen electrode after discharging can be quantitatively analyzed according to the maximum absorbance of H₂ [Ti(O₂) (SO₄)₂] at 408 nm in the UV–Vis spectrum [23]. Four different batches of TiOSO₄ solutions with the same volume were added with commercial Li₂O₂ of different qualities, and then tested with UV–Vis. The results obtained were shown in Figs. S18a and b). It can be found that the amount of commercial Li₂O₂ is linearly related to the intensity of absorbance. The amount of Li₂O₂ generated on the discharged electrodes can be calculated based on the fitted linear equation, as shown in Fig. S18b.

Fig. 7a and b are UV–Vis spectra of TiOSO_4 solution immersed with Pd– MoSe_2 electrodes and fitted plot between the absorbance and discharge capacity of the Pd– MoSe_2 electrode. Furthermore, the photo of the TiOSO_4 solution immersed with Pd– MoSe_2 oxygen electrodes clearly show that the color of the solution becomes darker as the discharge specific capacity is increased. The corresponding mass and yield of Li_2O_2 can be obtained by bringing the absorbance at different discharge capacities of the discharged electrode into the linear equation obtained in Fig. S18b. As shown in Table S7, the main discharge product of the Pd– MoSe_2 electrode is Li_2O_2 and the yield is about 67%.

In this case, Fig. 8 schematically shows the pathway of the reversible generation and decomposition of the Li_2O_2 on the Pd– MoSe_2 electrode. Generally, the charge and discharge process of oxygen electrodes in LOBs includes the internal migration of Li^+ and electrons, and the redox reaction on the catalyst surface. During the discharge process, O_2 dissolved in electrolyte is adsorbed on the surface of the Pd– MoSe_2 oxygen electrode to form adsorbed oxygen (O_2^*), then the O_2^* is reduced to form Li_2O_2 deposited on electrode surface [47,48]. During the charging process, Li_2O_2 loses electrons and oxidizes to O_2 , and Li^+ is released from the surface of Li_2O_2 . The rapid electron transport of Pd– MoSe_2 surface has a positive effect on the nucleation and growth of Li_2O_2 on the surface of the oxygen electrode. In addition, the electron density of MoSe_2 catalytic sites is adjusted by Pd atom, which indirectly promotes the desorption of O_2^* to generate free O_2 during charging. This has an important effect on the reversible formation and decomposition of Li_2O_2 . Moreover, because there is certain amount of Se vacancies on the surface of Pd– MoSe_2 , the electrons around the vacancies will delocalize, thereby further reducing the Li^+ /electron transport resistance.

4. Conclusion

In summary, atomic level Pd doping was exploited to improve the catalytic activity of MoSe_2 through thermodynamic spontaneous interfacial redox reaction. Partial Mo in MoSe_2 was replaced by Pd, which then covalently bonded with Se atoms, resulting in the formation of Se vacancies and enhancing the catalytic activity of Pd– MoSe_2 . By rationally controlling the surface electron density of the catalytic sites, the electronic properties of Pd– MoSe_2 can be effectively adjusted, which not only promotes the decomposition of Li_2O_2 , but also facilitates the desorption of O_2^* from the catalyst surface. Experimental results show that LOB with Pd– MoSe_2 electrode demonstrates low overpotential (0.47 V), high Coulombic efficiency (97.81%), and long cycle life (122 cycles) as compared to LOB with MoSe_2 electrode. Therefore, metal heteroatom doping provides a valuable strategy for developing highly efficient advanced catalysts for LOBs.

CRediT authorship contribution statement

Minglu Li: Methodology, Software, Data curation, Writing - original draft, preparation, Writing - review & editing. **Chaozhu Shu:** Conceptualization, Validation, Visualization, Preparation, Investigation, Supervision, Project administration, Funding acquisition. **Anjun Hu:** Supervision, Resources, Formal analysis, Investigation. **Jiabao Li:** Supervision, Resources. **Yu Yan:** Formal analysis, Supervision, Software. **Miao He:** Supervision, Resources, Formal analysis. **Jianping Long:** Visualization, Preparation, Project administration, Funding acquisition.

Declaration of competing interest

The authors declare that they have no known competing

financial interests or personal relationships that could have appeared to influence the work reported in this paper.

Acknowledgements

This work was financially supported by National Natural Science Foundation of China (No. 21905033), the Science and Technology Department of Sichuan Province (No. 2019YJ0503), and State Key Laboratory of Vanadium and Titanium Resources Comprehensive Utilization (No. 2020P4FZG02A).

Appendix A. Supplementary data

Supplementary data to this article can be found online at <https://doi.org/10.1016/j.jallcom.2020.157484>.

References

- [1] C. Shu, J. Wang, J. Long, H. Liu, S. Dou, Understanding the reaction chemistry during charging in aprotic lithium–oxygen batteries: existing problems and solutions, *Adv. Mater.* 31 (2019) 1804587.
- [2] J. Shen, H. Wu, W. Sun, J. Qiao, H. Cai, Z. Wang, In-situ nitrogen-doped hierarchical porous hollow carbon spheres anchored with iridium nanoparticles as efficient cathode catalysts for reversible lithium–oxygen batteries, *Chem. Eng. J.* 358 (2019) 340–350.
- [3] R. Bi, G. Liu, C. Zeng, X. Wang, L. Zhang, S. Qiao, 3D hollow α - MnO_2 framework as an efficient electrocatalyst for lithium–oxygen batteries, *Small* 15 (2019) 1804958.
- [4] A.J. Hu, M.J. Zhou, T.Y. Lei, Y. Hu, X.C. Du, C.H. Gong, C.Z. Shu, J.P. Long, J. Zhu, W. Chen, X.F. Wang, J. Xiong, Optimizing redox reactions in aprotic lithium–sulfur batteries, *Adv. Energy Mater.* (2020) 2002180.
- [5] L. Li, W. Han, L.J. Pi, P. Niu, J.B. Han, C.L. Wang, Emerging in-plane anisotropic two-dimensional materials, *Info 1* (2019) 54–73.
- [6] B. Liu, Y. Sun, L. Liu, S. Xu, X. Yan, Advances in manganese-based oxides cathodic electrocatalysts for Li–air batteries, *Adv. Funct. Mater.* 28 (2018) 1704973.
- [7] Y. Yin, Y. Zhang, T. Gao, T. Yao, X. Zhang, J. Han, Synergistic phase and disorder engineering in 1T– MoSe_2 nanosheets for enhanced hydrogen-evolution reaction, *Adv. Mater.* 29 (2017) 1700311.
- [8] J. Li, H. Hu, F. Qin, P. Zhang, L. Zou, H. Wang, Flower-like MoSe_2/C composite with expanded (0 0 2) planes of few-layer MoSe_2 as the anode for high-performance sodium-ion batteries, *Chem. Eur. J.* 23 (2017) 14004–14010.
- [9] L. Xing, X. Yan, J. Zheng, G. Xu, Z. Lu, L. Liu, Highly crystalline ReSe_2 atomic layers synthesized by chemical vapor transport, *Info 1* (2019) 552–558.
- [10] X.L. Wen, Z.B. Gong, D.H. Li, Nonlinear optics of two-dimensional transition metal dichalcogenides, *Info 1* (2019) 317–337.
- [11] D. Kong, H. Wang, J. Cha, M. Pasta, K. Koski, J. Yao, Synthesis of MoS_2 and MoSe_2 films with vertically aligned layers, *Nano Lett.* 13 (2013) 1341–1347.
- [12] C. Yang, Y. Yin, Y. Guo, Elemental selenium for electrochemical energy storage, *J. Phys. Chem. Lett.* 6 (2015) 256–266.
- [13] A. Eftekhari, Molybdenum diselenide (MoSe_2) for energy storage, catalysis, and optoelectronics, *Appl. Mater.* Today 8 (2017) 1–17.
- [14] Y.L. Guo, B. Wang, X.W. Zhang, S.J. Yuan, L. Ma, J.L. Wang, Magnetic two-dimensional layered crystals meet with ferromagnetic semiconductors, *Info 2* (2020) 639–655.
- [15] J.Y. Zhang, Y. Yu, P. Wang, C. Luo, X. Wu, Z.Q. Sun, Characterization of atomic defects on the photoluminescence in two-dimensional materials using transmission electron microscope, *Info 1* (2019) 85–97.
- [16] K. Zhang, Y. Li, S. Deng, S. Shen, Y. Zhang, G. Pan, Molybdenum selenide electrocatalysts for electrochemical hydrogen evolution reaction, *ChemElectroChem* 6 (2019) 3530–3548.
- [17] Z. Zhao, H. Zhang, H. Yuan, S. Wang, Y. Lin, Q. Zeng, Pressure induced metallization with absence of structural transition in layered molybdenum diselenide, *Nat. Commun.* 6 (2015) 7312.
- [18] S. Grigoriev, V. Fominski, R. Romanov, M. Volosova, A. Shelyakov, Pulsed laser deposition of nanocomposite MoSe_x/Mo thin-film catalysts for hydrogen evolution reaction, *Thin Solid Films* 592 (2015) 175–181.
- [19] X. Zhou, J. Jiang, T. Ding, J. Zhang, B. Pan, J. Zuo, Fast colloidal synthesis of scalable Mo-rich hierarchical ultrathin MoSe_{2-x} nanosheets for high-performance hydrogen evolution, *Nanoscale* 6 (2014) 11046–11051.
- [20] Z. Luo, Y. Ouyang, H. Zhang, M. Xiao, J. Ge, Z. Jiang, Chemically activating MoS_2 via spontaneous atomic palladium interfacial doping towards efficient hydrogen evolution, *Nat. Commun.* 9 (2018) 2120.
- [21] J. Kang, Q. Su, H. Feng, P. Huang, G. Du, B. Xu, MoSe_2 nanosheets-wrapped flexible carbon cloth as binder-free anodes for high-rate lithium and sodium ion storages, *Electrochim. Acta* 301 (2019) 29–38.
- [22] Y. Yu, G. Nam, Q. He, X. Wu, K. Zhang, Z. Yang, High phase-purity 1T'– MoSe_2 and 1T'– MoSe_2 layered crystals, *Nat. Chem.* 10 (2018) 638.
- [23] J. Li, C. Shu, A. Hu, Z. Ran, M. Li, R. Zheng, Tuning oxygen non-stoichiometric

- surface via defect engineering to promote the catalysis activity of Co_3O_4 in Li-O_2 batteries, *Chem. Eng. J.* 381 (2020) 122678.
- [24] Y. Zhang, Y. Liu, M. Ma, X. Ren, Z. Liu, G. Du, A Mn-doped Ni_2P nanosheet array: an efficient and durable hydrogen evolution reaction electrocatalyst in alkaline media, *Chem. Commun.* 53 (2017) 11048–11051.
- [25] K. Fan, H. Chen, Y. Ji, H. Huang, P. Claesson, Q. Daniel, Nickel–vanadium monolayer double hydroxide for efficient electrochemical water oxidation, *Nat. Commun.* 7 (2016) 11981.
- [26] Y. Yan, J. Lin, J. Cao, S. Guo, X. Zheng, J. Feng, J. Qi, Activating and optimizing activity of NiCoP nanosheets for electrocatalytic alkaline water splitting through V doping effect enhanced by P vacancies, *J. Mater. Chem.* 7 (2019) 24486–24492.
- [27] H. Moghaddam, H. Beitollahi, S. Tajik, M. Malakootian, H. Malen, Simultaneous determination of hydroxylamine and phenol using a nanostructure-based electrochemical sensor, *Environ. Monit. Assess.* 186 (2014) 7431–7441.
- [28] H. Beitollahi, I. Sheikhshoae, Novel nanostructure-based electrochemical sensor for simultaneous determination of dopamine and acetaminophen, *Mater. Sci. Eng. C* 32 (2012) 375–380.
- [29] H. Beitollahi, M. Safaei, S. Tajik, Different electrochemical sensors for determination of dopamine as neurotransmitter in mixed and clinical samples: a review, *Anal. Bioanal. Chem. Res.* 6 (2019) 81–96.
- [30] A. Khalilzadeh, S. Tajik, H. Beitollahi, R. Venditti, Green synthesis of magnetic nanocomposite with iron oxide deposited on cellulose nanocrystals with copper ($\text{Fe}_3\text{O}_4@\text{CNC}/\text{Cu}$): investigation of catalytic activity for the development of a venlafaxine electrochemical sensor, *Ind. Eng. Chem. Res.* 59 (2020) 4219–4228.
- [31] M. Mazloun-Ardakani, H. Beitollahi, M. Amini, B. Mirjalili, F. Mirkhalaf, Simultaneous determination of epinephrine and uric acid at a gold electrode modified by a 2-(2,3-dihydroxy phenyl)-1, 3-dithiane self-assembled monolayer, *J. Electroanal. Chem.* 651 (2011) 243–249.
- [32] H. Soltani, H. Beitollahi, A. Hatefi-Mehrjardi, S. Tajik, M. Torkzadeh-Mahani, Voltammetric determination of glutathione using a modified single walled carbon nanotubes paste electrode, *Anal. Bioanal. Chem.* 6 (2014) 67–79.
- [33] J. Zhang, T. Wang, P. Liu, Y. Liu, J. Ma, D. Gao, Enhanced catalytic activities of metal-phase-assisted 1T@2H- MoSe_2 nanosheets for hydrogen evolution, *Electrochim. Acta* 217 (2016) 181–186.
- [34] R. Wei, X. Bu, W. Gao, R. Villaos, G. Macam, Z. Huang, Engineering surface structure of spinel oxides via high-valent vanadium doping for remarkably enhanced electrocatalytic oxygen evolution reaction, *ACS Appl. Mater. Interfaces* 11 (2019) 33012–33021.
- [35] A. Hu, C. Shu, C. Xu, J. Li, R. Liang, R. Zheng, Interface-engineered metallic 1T- MoS_2 nanosheet array induced via palladium doping enabling catalysis enhancement for lithium–oxygen battery, *Chem. Eng. J.* 382 (2020) 122854.
- [36] X. Zhang, S. Hu, Y. Zheng, R. Wu, F. Gao, P. Yang, et al., Polymorphic cobalt diselenide as extremely stable electrocatalyst in acidic media via a phase-mixing strategy, *Nat. Commun.* 5338 (2019).
- [37] D. Yan, Y. Li, J. Huo, R. Chen, L. Dai, S. Wang, Defect chemistry of nonprecious-metal electrocatalysts for oxygen reactions, *Adv. Mater.* 29 (2017) 1606459.
- [38] Y. Zhao, C. Zhang, R. Fan, J. Li, Y. Hao, J. He, Selenium decorated reduced graphene oxide supported CoSe_2 nanoparticles as efficient electrochemical catalyst for the oxygen reduction reaction, *ChemElectroChem* 5 (2018) 3287–3292.
- [39] N. Yao, P. Li, Z. Zhou, Y. Zhao, G. Cheng, S. Chen, Synergistically tuning water and hydrogen binding abilities over Co_4N by Cr doping for exceptional alkaline hydrogen evolution electrocatalysis, *Adv. Energy Mater.* 9 (2019) 1902449.
- [40] X. Zheng, Z. Guo, G. Zhang, H. Li, J. Zhang, Q. Xu, Building a lateral/vertical 1T-2H MoS_2/Au heterostructure for enhanced photoelectrocatalysis and surface enhanced Raman scattering, *J. Mater. Chem.* 7 (2019) 19922–19928.
- [41] K. Yoon, K. Shin, J. Park, S. Cho, C. Kim, J. Jung, Brush-like cobalt nitride anchored carbon nanofiber membrane: current collector-catalyst integrated cathode for long cycle Li-O_2 batteries, *ACS Nano* 12 (2017) 128–139.
- [42] J. Li, C. Shu, Z. Ran, M. Li, R. Zheng, J. Long, Heteroatom-induced electronic structure modulation of vertically oriented oxygen vacancy-rich NiFe layered double oxide nanoflakes to boost bifunctional catalytic activity in Li-O_2 battery, *ACS Appl. Mater. Interfaces* 11 (2019) 29868–29878.
- [43] L. Shang, H. Yu, X. Huang, T. Bian, R. Shi, Y. Zhao, Well-dispersed ZIF-derived Co , N-Co-doped carbon nanoframes through mesoporous-silica-protected calcination as efficient oxygen reduction electrocatalysts, *Adv. Mater.* 28 (2016) 1668–1674.
- [44] B. Adams, C. Radtke, R. Black, M. Trudeau, K. Zaghib, L. Nazar, Current density dependence of peroxide formation in the Li-O_2 battery and its effect on charge, *Energy Environ. Sci.* 6 (2013) 1772–1778.
- [45] B. Kim, H. Kim, S. Back, K. Nam, Y. Jung, Y. Han, Improved reversibility in lithium-oxygen battery: understanding elementary reactions and surface charge engineering of metal alloy catalyst, *Sci. Rep.* 4 (2014) 4225.
- [46] K. Yao, D. Kwabi, R. Quinlan, N. Mansour, A. Grimaud, Y. Lee, Thermal stability of Li_2O_2 and Li_2O for Li-air batteries: in situ XRD and XPS studies, *J. Electrochem. Soc.* 160 (2013) A824–A831.
- [47] A. Hu, J. Long, C. Shu, C. Xu, T. Yang, R. Liang, Three-dimensional CoNi_2S_4 nanorod arrays anchored on carbon textiles as an integrated cathode for high-rate and long-life lithium–oxygen battery, *Electrochim. Acta* 301 (2019) 69–79.
- [48] A. Hu, W. Lv, T. Lei, W. Chen, Y. Hu, C. Shu, Heterostructured $\text{NiS}_2/\text{ZnIn}_2\text{S}_4$ realizing toroid-like Li_2O_2 deposition in lithium-oxygen batteries with low-donor-number solvents, *ACS Nano* 14 (2020) 3490–3499.